

# Chandra Observations of A2670 and A2107: A Comet Galaxy and cDs with Large Peculiar Velocities

Yutaka FUJITA<sup>1</sup> Craig L. SARAZIN<sup>2</sup> and Gregory R. SIVAKOFF<sup>2</sup>

<sup>1</sup>*Department of Earth and Space Science, Graduate School of Science,  
Osaka University, Toyonaka, Osaka 560-0043*

*fujita@vega.ess.sci.osaka-u.ac.jp*

<sup>2</sup>*Department of Astronomy, University of Virginia,  
P. O. Box 3818, Charlottesville, VA 22903-0818, USA*

(Received 2000 January 1; accepted 2000 January 1)

## Abstract

We present an analysis of Chandra observations of the galaxy clusters A2670 and A2107. Their cD galaxies have large peculiar velocities ( $> 200 \text{ km s}^{-1}$ ) and thus the clusters appear to be undergoing mergers. In A2670, we find a comet-like structure around one of the brightest galaxies. At the leading edge of the structure, there is a cold front. The mass of the X-ray gas in the comet-like structure suggests that the galaxy was in a small cluster or group, and its intracluster medium (ICM) is being stripped by ram-pressure. The regions of cool interstellar medium (ISM) of the cD galaxies in A2670 and A2107 are very compact. This is similar to the brightest galaxies in the Coma cluster, which is also a merging cluster. In each galaxy, the short cooling time of the ISM requires a heating source; the compact nature of the ISM makes it unlikely that the heating source is a central active galactic nucleus (AGN).

**Key words:** cooling flows — galaxies: clusters: general — galaxies: clusters: individual (A2107, A2670) — intergalactic medium — X-rays: galaxies: clusters

## 1. Introduction

It is generally believed that dark matter constitutes a large fraction of the mass in the Universe. Among various theories of dark matter, cold dark matter (CDM) theory provides a remarkably successful description of large-scale structure formation and is in good agreement with a large variety of observational data. This model predicts that small objects are the first to form and that these then amalgamate into progressively larger systems. In this model, clusters of galaxies are considered to be the objects that have recently formed via mergers of subclusters. A cluster merger is one of the most spectacular events in the Universe. In a major

merger, subclusters collide at velocities of  $\gtrsim 1000 \text{ km s}^{-1}$  and release gravitational energies of  $\sim 10^{64}$  erg.

A giant elliptical galaxy (cD galaxy) is often located at the center of a cluster. In general, the peculiar velocities of the cD galaxies are much smaller ( $\lesssim 200 \text{ km s}^{-1}$ ; Oegerle, Hill 2001) than the velocity dispersions of other galaxies in the clusters ( $\sim 1000 \text{ km s}^{-1}$ ). This means that the cD galaxies are nearly at rest in the cluster potential wells. However, the cD galaxies in some clusters have large peculiar velocities ( $\gtrsim 200 \text{ km s}^{-1}$ ). Since a cluster merger may disturb a cD galaxy from its resting place at the bottom of the potential, the large peculiar velocity of the cD galaxy is a good indicator of mergers.

In this paper, we present the results of Chandra observations of two clusters containing rapidly moving cD galaxies in order to study the effects of cluster mergers on the cluster galaxies (including the cD galaxies) and the nature of substructures within clusters. Recently, Oegerle and Hill (2001) studied the redshifts of cluster galaxies and their distributions intensively. They observed redshifts of 50–300 galaxies per cluster and studied the peculiar velocities of cD galaxies in the clusters. For several clusters, they compiled published data. Among 25 clusters, they found 4 clusters for which the redshifts of the cD galaxies are significantly different from the cluster means within  $1.5 h_{75}^{-1}$  Mpc of the cDs, where the Hubble constant is  $H_0 = 75 h_{75} \text{ km s}^{-1} \text{ Mpc}^{-1}$ . The clusters are A2052, A2107, A2199, and A2670. The peculiar velocities of the cD galaxies are  $\sim 250\text{--}400 \text{ km s}^{-1}$ . Among them, A2052 and A2199 have already been observed by Chandra. For these clusters, although interesting X-ray structures are observed in the cluster cores, no X-ray features related to the motion of the cD galaxies have been reported (Blanton et al. 2001; Johnstone et al. 2002; Kawano et al. 2003).

In this paper, we report on Chandra X-ray observations of the remaining two clusters that have fast moving cDs, A2107 and A2670. The peculiar velocities of the cD galaxies are  $v_p = 433 \text{ km s}^{-1}$  for A2670, and  $270 \text{ km s}^{-1}$  for A2107 (Oegerle, Hill 2001). For A2670, Hobbs and Willmore (1997) analyzed the existing X-ray and optical data. While the X-ray morphology on large scales is regular, the cluster has complicated structures at the center. Hobbs and Willmore (1997) detected four point sources near the center of the ROSAT HRI image as is shown in their figure 2. Besides the cD galaxy, they argued that two of the sources (1:  $23^{\text{h}}54^{\text{m}}09^{\text{s}}.5$ ,  $-10^{\circ}25'48''$ , and 3:  $23^{\text{h}}54^{\text{m}}07^{\text{s}}.0$ ,  $-10^{\circ}25'17''$ ) were coincident with cluster galaxies. The X-ray contours near the cluster center are elongated towards east and west, which suggests that the cD galaxy and sources 1 and/or 3 are interacting. Bird (1994) indicated that the cluster consists of four subclumps from the spatial and redshift distributions of the galaxies. The centers of three subclumps (Clumps A, B, and C) are very close to the cluster center (within a few arcminutes from the cD galaxy). This may show that these subclumps are near their point of closest approach to one another. Bird (1994) showed that the masses of the subclumps are comparable; the subclumps may induce strong gas motion in the hot intracluster medium (ICM). On the other hand, the X-ray morphology of A2107 is not reported to be irregular

(Buote, Tsai 1996), although the detailed X-ray structures in the central region have not been investigated. Both A2670 and A2107 have relatively weak central X-ray peaks, which may show that the gas motions in the ICM disrupt the central gas structures of the clusters. In terms of classical cooling flows, their peak strengths are equivalent to the mass deposition rates of  $\dot{M} \lesssim 50 M_{\odot} \text{yr}^{-1}$  (White et al. 1997), although the classical cooling flow model is no longer valid (Makishima et al. 2001; Peterson et al. 2001; Kaastra et al. 2001; Tamura et al. 2001).

In the following analysis, we use the cosmological parameters of  $\Omega_0 = 0.27$ ,  $\lambda = 0.73$ , and the Hubble constant of  $H_0 = 70 \text{ km s}^{-1} \text{ Mpc}^{-1}$  unless otherwise mentioned. This means that  $1''$  corresponds to 1.45 kpc for A2670 ( $z = 0.0765$ ) and 0.813 kpc for A2107 ( $z = 0.0411$ ).

## 2. Observations and Data Analysis

A2670 and A2107 were observed with Chandra on 2004 May 10 for a total of 40 ks and on 2004 September 7 for a total of 36 ks, respectively. The data were taken in Very Faint mode using the four ACIS-I chips and the S2 chip, with the cluster center located on the ACIS-I detector. The focal plane temperature was  $-120 \text{ C}$ , and only events with ASCA grades of 0, 2, 3, 4, and 6 were analyzed. We used the data analysis package CIAO, version 3.1, for the data reductions. Background files were taken from the blank-sky observations compiled by M. Markevitch<sup>1</sup> and included in the CIAO calibration database (CALDB 2.26). We searched for background flares using data from the S2 chip, since the cluster emission fills the ACIS-I chips. We used the script `lc_clean` to clean the data in the same manner as was done by M. Markevitch for the blank-sky fields. After flare removal, the useful exposures were 26 ks for A2670 and 30 ks for A2107. The background files were normalized by requiring the same event count rate as the data in a hard band (PHA channels between 2500 and 3000). We did not find any excess soft X-ray background in the direction of either cluster (i.e., Vikhlinin et al. 2005).

## 3. X-ray Images

Figure 1 shows the combined ACIS-I images of A2670 and A2107 in the 0.3–10 keV energy band. In figure 1a, the positions of the subclumps in A2670 identified by Bird (1994) through galaxy motions are shown. The centers of the clumps are determined by galaxy positions and the errors may be very large. Figure 2 shows the X-ray images of the central regions of the two clusters. The images were smoothed using the CIAO routine ‘`csmooth`’. The images have a minimum signal-to-noise ratio of 3 per smoothing beam and were corrected for exposure, vignetting, and background. In figure 3, contours from the X-ray images are superposed on the Digital Sky Survey (DSS) images of the two clusters.

In A2670 (figure 2a), the bright source at the center of the X-ray image corresponds to the cD galaxy near the center of the cluster (figure 3a). The spatial size of the brightest X-ray

<sup>1</sup> <http://cxc.harvard.edu/contrib/maxim/bg/>

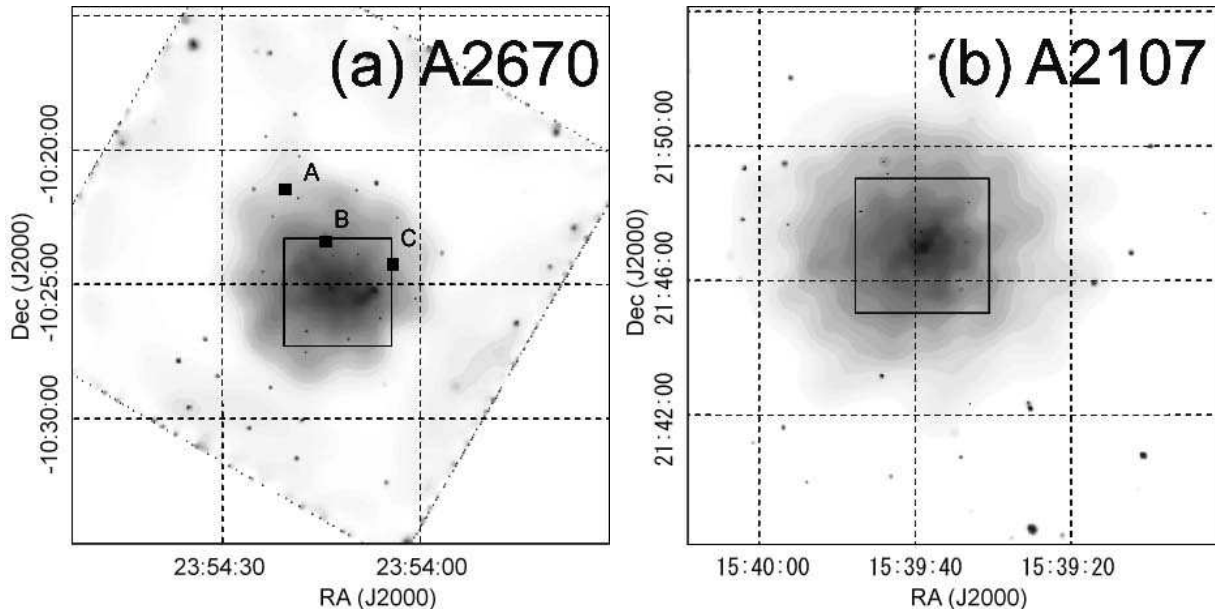


**Fig. 1.** Adaptively smoothed, combined ACIS-I images of (a) A2670 and (b) A2107 in the energy range of 0.3–10 keV, corrected for background, exposure, and vignetting. The regions shown in figure 2 are indicated as solid-line squares. The filled squares in figure 1a are the positions of the subclumps identified by Bird (1994). Clump D found by Bird (1994) is outside this figure.

region of the cD galaxy is much smaller than those of cD galaxies in most cooling core clusters. The radius is only  $\sim 4$  kpc and is smaller than the optical size of the cD galaxy (figure 3a). The X-ray source associated with the cD was also seen in the ROSAT HRI image (Hobbs, Willmore 1997).

In figure 2a, a comet-like X-ray feature is seen to the west of the cD galaxy in A2670. The tail of the comet extends from the elliptical galaxy 2MASX J23540700–1025169, which is located at the bright source at the head of the comet (figure 3a). This X-ray source corresponds with source 3 in figure 2 in Hobbs and Willmore (1997). We will refer to this X-ray comet and the associated galaxy as the ‘comet galaxy’ from now on. Although the leading edge of the comet corresponds to a steep gradient in the X-ray surface brightness, which we will argue is a cold front (section 5.1 below), there is no clear indication of a bow shock ahead of the galaxy. We did not find point sources at the locations of sources 1 and 2 ( $23^{\text{h}}54^{\text{m}}08^{\text{s}}.2$ ,  $-10^{\circ}25'37''$ ) found by Hobbs and Willmore (1997) in the ROSAT HRI image. Instead, it appears likely that these “sources” are just the comet tail in the Chandra image. The Chandra image of A2670 also shows an extension to the northeast of the cD, which might be associated with galaxy groups A and B in Bird (1994).

Compared with A2670, the overall structure of A2107 is more regular (figure 1b). However, the ICM in the central region ( $\lesssim 15''$  from the center) has an irregular structure (figure 2b). This corresponds to the region around the central cD galaxy (figure 3b). One interesting feature is that the X-ray emission at the center of the cD is elongated roughly east-

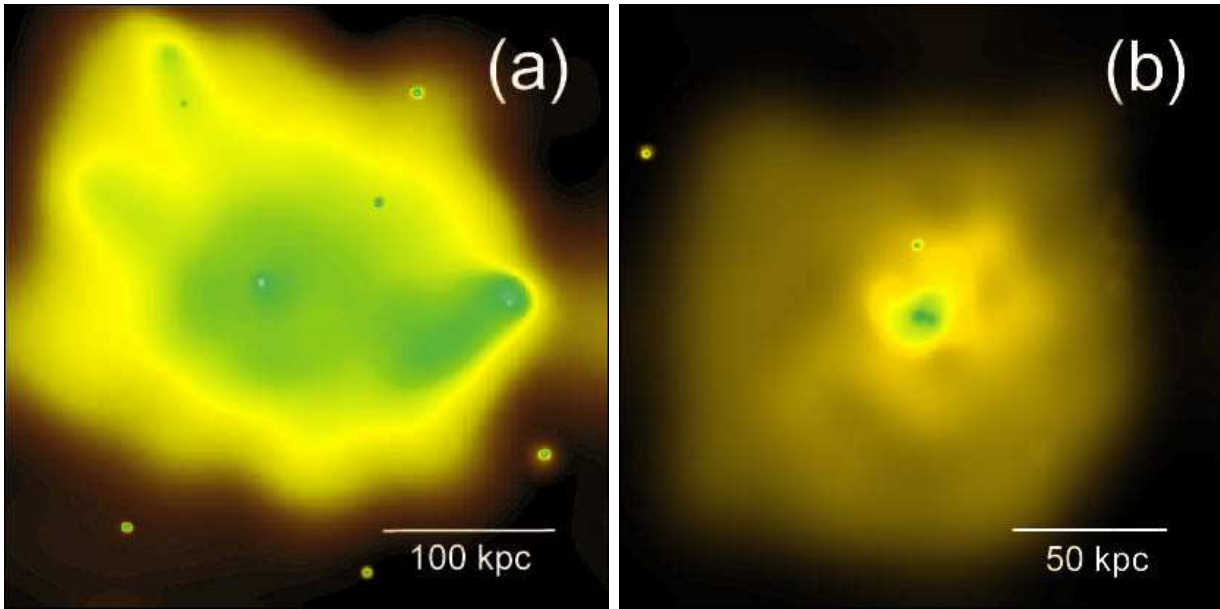


**Fig. 2.** Adaptively smoothed Chandra images of the central  $4' \times 4'$  regions of (a) A2670 and (b) A2107, corrected for background, exposure, and vignetting.

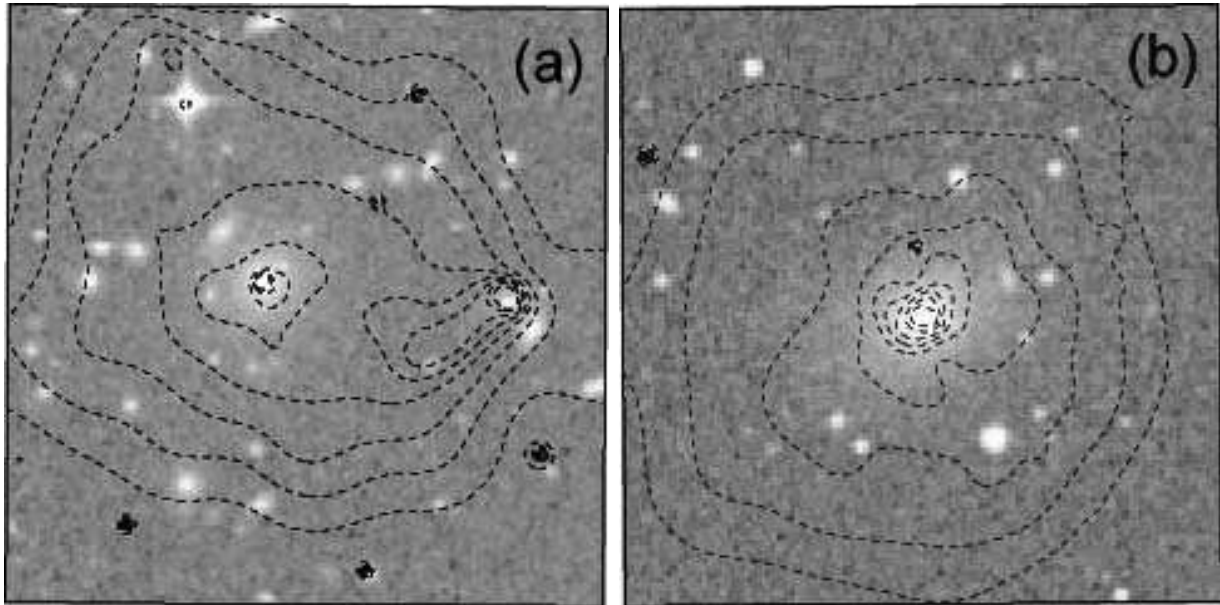


**Fig. 3.** X-ray brightness contours (0.3–10 keV band, logarithmically spaced by a factor of  $\sqrt{2}$ ), overlaid on the DSS optical images of the central  $4' \times 4'$  regions of (a) A2670 and (b) A2107. Contours at the very centers of the cDs and comet galaxy are omitted to see the optical images.

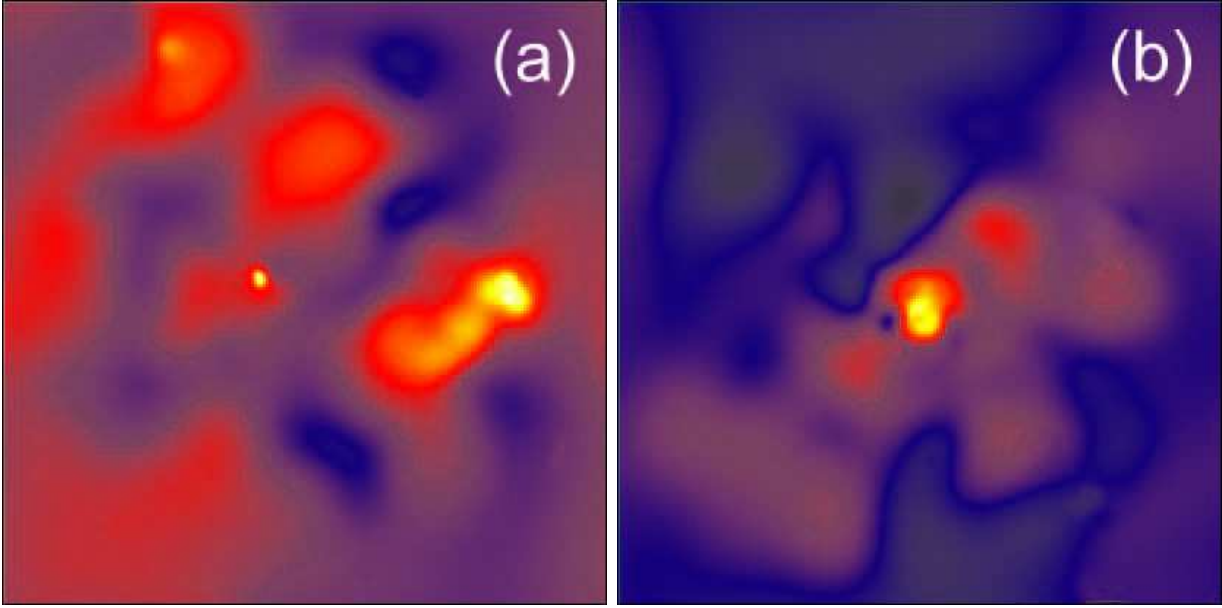


**Fig. 4.** Color maps of hardness ratio of the central  $4' \times 4'$  regions of (a) A2670 and (b) A2107, based on the ratio of the count rates in the energy bands 2.0–10 and 0.3–2.0 keV. The hardness ratios are corrected for background, exposure, and vignetting and are adaptively smoothed. Soft emission appears yellow and hard emission blue. Before taking the ratio, the hard and soft images were respectively smoothed using the same scale map (0.3–10 keV). Note that the color scales are different between (a) and (b). Deep blue is a hardness ratio of 0.47 and 0.55, and bright yellow is 0.10 and 0.22 for A2670 and A2107, respectively. Point sources are removed.

west (green color in figure 2b). The optical center of the cD galaxy is at the center of the elongated structure.

Figure 4 shows hardness ratio maps of A2670 and A2107, which are made in order to choose regions for spectral analysis (section 4). We define the hardness ratio as the count rate in the 2–10 keV band divided by the count rate in the 0.3–2 keV band. The blue color indicates hard X-ray emission, while the yellow color is the softest emission. The regions shown are the same as in figures 2 and 3.

In A2670, the X-ray excess corresponding to the cD galaxy is soft. The head of the comet associated with the comet galaxy is also distinctively soft. Although it is not as soft as the emission from the two galaxies, the tail of the comet appears to be softer than the surrounding hot ICM. The softer X-ray emission from these regions is due to cooler gas than that in the surrounding cluster (section 4 below).

In the central region of A2107, the structures seen in the hardness ratio map for the central  $\sim 15''$  region are different from those seen in the X-ray image (figure 2b). In the X-ray image, the emission is elongated east-west, which is also shown by the innermost contours in figure 3b. Presumably, the X-ray image shows where the densest gas is located. In the hardness ratio map (figure 4), the softest (and presumably coolest) gas is elongated north-south. The difference of structure between figures 2 and 4 suggests that the cluster center is not in pressure

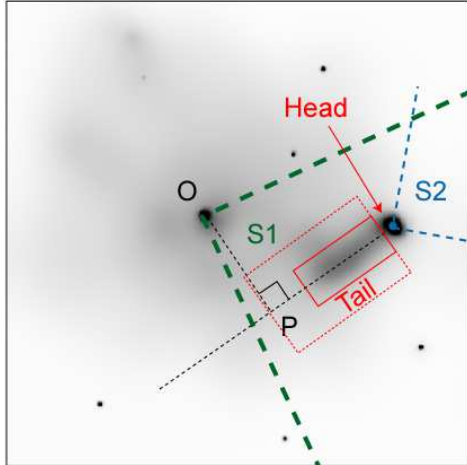


**Fig. 5.** X-ray image of the center of A2670, with several regions for further analysis indicated. The image is a grey-scale version of figure 2a. The sectors S1 and S2 are indicated by bold and thin dashed lines, respectively.

equilibrium; the denser gas does not always correspond to the cooler gas, especially in the azimuthal direction. Similar structures have been found in the centers of a few other clusters, including AWM7 (Furusho et al. 2003) and 2A0335+096 (Mazzotta et al. 2003).

The radial X-ray surface brightness profile of each of the clusters was determined by accumulating counts in circular annuli. The profiles were centered on the peaks in the X-ray surface brightness coincident with the X-ray centers of the cD galaxies. For A2670, the  $90^\circ$  sector including the comet galaxy (S1 in figure 5) was excluded from the surface brightness profile. The counts in annuli were corrected for background, vignetting, and exposure. The resulting surface brightness profiles are shown in figure 6. We first tried to fit a single  $\beta$  model to the surface brightness profiles, but the fits were not acceptable. Figure 6 suggests that there are two components to the surface brightness of each cluster. Thus, we fit the radial profiles of the surface brightness with double  $\beta$  model functions

$$S_X(R) = S_{0,1} \left( 1 + \frac{R^2}{r_{c1}^2} \right)^{-3\beta_1+1/2} + S_{0,2} \left( 1 + \frac{R^2}{r_{c2}^2} \right)^{-3\beta_2+1/2}, \quad (1)$$

where  $R$  is the projected distance from the cluster center. This fit yields values for the core radii  $r_{c1}$  and  $r_{c2}$ , the  $\beta$  parameters  $\beta_1$  and  $\beta_2$ , and the normalizations  $S_{0,1}$  and  $S_{0,2}$ . We adopted the double  $\beta$  model functions because they are easily converted into a density profile (see equation [2]). The best-fit parameters are given in table 1, and the best-fit total model profiles and individual components are shown in figure 6.

The core radii of the inner components of both clusters are very small ( $\sim 3$  kpc). This is much smaller than any characteristic scale expected to be associated with a cluster of galaxies, and thus we will assume that these components are associated with the central cD galaxies.

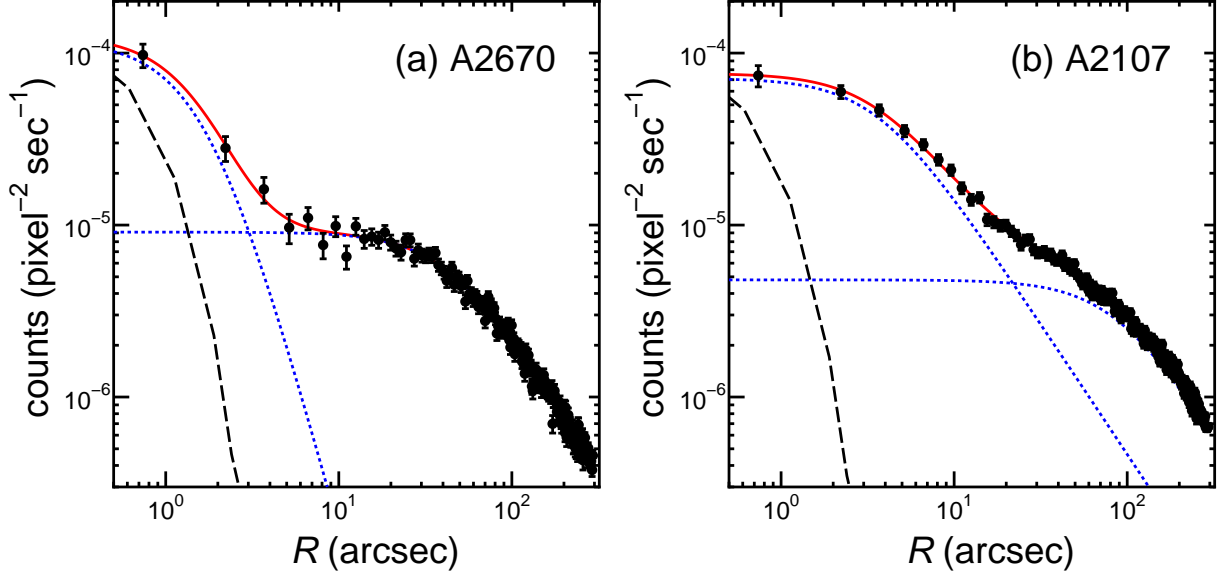


**Fig. 6.** Surface brightnesses as a function of radius for (a) A2670 excluding the  $90^\circ$  sector including the comet galaxy (S1 in figure 5) and (b) A2107 for 0.3–10 keV. Error bars are  $1\sigma$  Poisson uncertainties. The results of double  $\beta$  model fits are shown by solid lines. The contribution of each  $\beta$  model is shown by dotted lines. The dashed lines show the expected radial profile for a point source.

**Table 1.** Parameters for  $\beta$  model fits

Cluster	$r_{c1}$ (kpc)	$r_{c2}$ (kpc)	$\beta_1$	$\beta_2$	$S_{0,1}$ ( $10^{-5} \text{cnts s}^{-1} \text{pix}^{-2}$ )	$S_{0,2}$ ( $10^{-5} \text{cnts s}^{-1} \text{pix}^{-2}$ )
A2670 (Excluding Comet*)	$2.55^{+1.28}_{-1.28}$	$66.0^{+3.2}_{-3.2}$	$0.79^{+0.29}_{-0.29}$	$0.44^{+0.01}_{-0.01}$	$11.8^{+3.3}_{-3.3}$	$0.91^{+0.03}_{-0.03}$
A2670 (Comet Direction <sup>†</sup> )	$11.3^\ddagger$	...	$0.49^{+0.01}_{-0.01}$	...	$38.3^{+8.5}_{-8.5}$	...
A2170	$3.15^{+0.67}_{-0.67}$	$78.8^{+11.7}_{-11.7}$	$0.42^{+0.04}_{-0.04}$	$0.44^{+0.02}_{-0.02}$	$7.14^{+0.81}_{-0.81}$	$0.48^{+0.01}_{-0.01}$

\* Excluding the  $90^\circ$  sector including the comet galaxy (outside S1 in Fig. 5).

<sup>†</sup> The  $90^\circ$  sector including the comet galaxy (S1 in Fig. 5, see section 4.2.2). Single  $\beta$  model fit.

<sup>‡</sup> Fixed.

Even with that assumption, these core radii are small. On the other hand, the central components are clearly resolved; thus, they are not point sources associated with central AGNs in the cD galaxies. The dashed lines in figure 6 show the point-spread-function for a source with a spectrum similar to that of the central emission. A careful examination of the raw data images shows no evidence for an unresolved point source at the center of either cD galaxies. Thus, it is likely that these central components are emission from highly compressed gas. The outer core radii are similar to the sizes of cooling cores seen in relaxed clusters.

#### 4. Spectral Analysis

We extracted spectra in the 0.3–10 keV band in PI channels from selected regions of the Chandra images using the CIAO software package. Both the response matrix files and the ancillary response files were calculated using the MKRMF/MKWARF package. The package



**Table 2.** X-ray Spectra of A2670 and A2107

Region (Model)	Radius	$T$ (keV)	$Z$ ( $Z_{\odot}$ )	$T_{\text{out}}$ (keV)	$N_{\text{H}}$ ( $10^{20} \text{ cm}^{-2}$ )	$\dot{M}$ ( $M_{\odot} \text{ yr}^{-1}$ )	$\chi^2/\text{dof}$
A2670, Global (1T)	4'92	$3.8^{+0.2}_{-0.2}$	$0.47^{+0.09}_{-0.08}$	...	$7.1^{+1.0}_{-1.0}$	...	0.979 (345.3/401)
A2670, Global (CF)	4'92	$3.9^{+0.2}_{-0.2}$	$0.42^{+0.08}_{-0.07}$	...	$6.9^{+1.2}_{-0.9}$	$0^{+11.7}_{-0}$	0.980 (343.8/400)
A2670, Comet Head (2T* )	8''9	$1.4^{+0.3}_{-0.1}$	$0.47^{\dagger}$	$4.7^{\ddagger}$	$7.1^{\dagger}$	...	0.570 (11.4/20)
A2670, Comet Head (2T* )	8''9	$1.6^{+0.2}_{-0.3}$	$1.0^{\dagger}$	$4.7^{\ddagger}$	$7.1^{\dagger}$	...	0.512 (10.2/20)
A2670, Comet Tail (2T* )	49'' $\times$ 22''	$1.5^{+0.6}_{-0.3}$	$0.47^{\dagger}$	$3.6^{\ddagger}$	$7.1^{\dagger}$	...	0.631 (29.0/46)
A2670, Comet Tail (2T* )	49'' $\times$ 22''	$1.7^{+0.5}_{-0.4}$	$1.0^{\dagger}$	$3.6^{\ddagger}$	$7.1^{\dagger}$	...	0.602 (27.7/46)
A2107, Global (1T)	4'92	$4.0^{+0.1}_{-0.1}$	$0.44^{+0.07}_{-0.06}$	...	$7.9^{+0.7}_{-0.7}$	...	0.896 (467.7/522)
A2107, Global (CF)	4'92	$4.1^{+0.2}_{-0.1}$	$0.39^{+0.06}_{-0.06}$	...	$7.8^{+0.9}_{-0.8}$	$1.1^{+3.8}_{-1.1}$	0.891 (464.0/521)

\* Deprojection.

$\dagger$  Assumed.

$\ddagger$  Fixed.

weighted the response files by the X-ray brightness over the corresponding image region. The spectra were grouped to have a minimum of 20 counts per bin and fitted with one or two thermal models using XSPEC, version 11.3.0. As a thermal model, we use APEC, unless otherwise mentioned. We also use WABS for absorption ( $N_{\text{H}}$ ). Errors on fitted spectral parameters are given at the 90% confidence level in this section.

#### 4.1. Global Spectrum

First, we studied the average spectra extracted from circular regions of 4'92 radius centered on the cD galaxies. The spectra can be reproduced by a single thermal component with absorption (1T models in table 2). For A2670, the temperature  $T$  is consistent with previous ROSAT and ASCA observations ( $3.7^{+0.3}_{-0.3}$  keV; Hobbs, Willmore 1997). The metal abundance obtained with Chandra (table 2) is larger than that obtained with ASCA ( $Z = 0.20^{+0.11}_{-0.09} Z_{\odot}$ ; Hobbs, Willmore 1997). One possible reason could be that the cluster has a metal abundance excess at the center like many other clusters (Fukazawa et al. 2000); since the field of view of Chandra is smaller than ASCA, the metal abundance measured with Chandra could be larger than that measured with ASCA. The absorption we obtain with Chandra (table 2) is larger than the Galactic value ( $N_{\text{H}} = 2.92 \times 10^{20} \text{ cm}^{-2}$ ; Stark et al. 1992) and that obtained with ROSAT ( $N_{\text{H}} = 3.6 \times 10^{20} \text{ cm}^{-2}$ ; Hobbs, Willmore 1997), although it is consistent with the ASCA result ( $N_{\text{H}} = 6^{+6}_{-5} \times 10^{20} \text{ cm}^{-2}$ ; Hobbs, Willmore 1997). The excess absorption exists even if we use ACISABS software. If the ROSAT result is correct, one possible reason of the discrepancy might be an imperfect correction of the quantum efficiency degradation of the ACIS detector on Chandra at low energies. Because of this possible source of uncertainty, we do not discuss  $N_{\text{H}}$  further. For A2107, the temperature obtained with Chandra is consistent with that obtained with Einstein MPC (4.1 keV; David et al. 1993). The best-fit absorption is larger than the Galactic value ( $N_{\text{H}} = 5.02 \times 10^{20} \text{ cm}^{-2}$ ; Stark et al. 1992).

We also fitted the global spectra with the MKCFLOW model based on the MEKAL

thermal model in order to estimate the emission from low temperature gas. Although this model may not give actual cooling rates if the standard cooling flow is wrong, it should give cooling rates at least qualitatively. Thus, the results would be useful to be compared with those of previous studies. We added a MEKAL model representing the emission outside the cooling core and a variable WABS absorption model ( $N_H$  in table 2). We fix the metal abundance and initial gas temperature in the MKCFLOW component to the values of abundance and temperature of the MEKAL component, respectively. The results are shown in table 2 as CF (for ‘cooling flow’) models. The mass deposition rates,  $\dot{M}$ , are very small and consistent with zero. We note that the results are not sensitive to the metal abundance of the MKCFLOW component; even if we assume that  $Z = 1 Z_\odot$  for the MKCFLOW component and if  $Z$  is not fixed for the MEKAL component, the results of spectral fits are almost the same.

#### 4.2. Individual Regions

Next, we studied spectra of individual regions. Unfortunately, total photon counts for both clusters are relatively small. Therefore, we only investigated the spectra of several interesting regions and fixed the metal abundance and the absorption at the values for the innermost 4:92 radius (1T models in table 2) unless otherwise mentioned.

##### 4.2.1. Temperature and Density Profiles

The hardness ratio maps show that the cluster centers (cD galaxies) are cooler than the surrounding regions (figure 4). Therefore, the effect of projection of the hotter outer gas onto the cooler central regions must be considered for the spectral analysis.

Based on the hardness ratio maps, we extracted the spectra from a few annular regions. In A2670, these annuli had projected radii of  $3'' < R < 260''$  (region 1) and  $0'' < R < 3''$  (region 2). The projected radii were  $15'' < R < 260''$  (region 1),  $7'' < R < 15''$  (region 2), and  $0'' < R < 7''$  (region 3) for A2107. (Further division of the regions gives spectra with too few counts to give meaningful constraints on the temperatures.) We assumed that the clusters are spherically symmetric, although the  $90^\circ$  sector including the comet galaxy (S1 in figure 5) is excluded for A2670. The spherical shells corresponding to the above annuli are numbered in a corresponding way.

Usual deprojection analysis assumes that both density and temperature within each spherical shell are constant (Blanton et al. 2001; Fujita et al. 2002). The hardness ratio map indicates that the assumption is not bad for temperature (figure 4). On the other hand, it is not appropriate for density, because the number of the shells is too small and thus the widths of the individual shells are too large to assume that. Therefore, we modified the usual deprojection analysis in the following way. In this analysis, we assumed that the temperature within each spherical shell is constant, but the density is not.

We assume that the X-ray surface brightness profile is given by the double  $\beta$  model fits in table 1. If the temperature is constant throughout the cluster, the double  $\beta$  model can be

deprojected to give the density profile

$$n_{\text{gas},i}(r)^2 = n_{\text{gas},1,i}^2 \left(1 + \frac{r^2}{r_{c1}^2}\right)^{-3\beta_1} + n_{\text{gas},2,i}^2 \left(1 + \frac{r^2}{r_{c2}^2}\right)^{-3\beta_2}, \quad (2)$$

where  $r$  is the radius from the cluster center. Here, since the temperature is assumed to be different in each shell, we assume the same form applies but with a different normalization for each shell  $i$ . That is, the parameters  $r_{c1}$ ,  $r_{c2}$ ,  $\beta_1$ , and  $\beta_2$ , are not dependent on the shell  $i$ , but  $n_{\text{gas},1,i}$  and  $n_{\text{gas},2,i}$  are. The normalization is chosen to be consistent with the observed surface brightness (table 1) and the emissivity resulting from the temperature in that shell. Thus, a temperature and a normalization are assigned to each shell in our procedure. (On the other hand, a temperature and an uniform density are assigned to each shell in the conventional deprojection method.) In other words, instead of the uniform density, we used the normalization of the density profile, fixing the functional form (the double  $\beta$  model). The individual normalizations  $n_{\text{gas},1,i}$  and  $n_{\text{gas},2,i}$  can be determined from the overall normalization of each shell, and the relation

$$n_{\text{gas},2,i} = \left(\frac{S_{0,2}r_{c1}}{S_{0,1}r_{c2}}\right)^{1/2} n_{\text{gas},1,i}. \quad (3)$$

Thus, the normalization is given by one parameter ( $n_{\text{gas},1,i}$ ). Note that although we use the results of double  $\beta$  model fits, we do not assume two-phase structure to the gas (two temperatures at a given radius). We adopted equation (2) just as a functional form for the X-ray surface brightness profile.

To include projection effects on the spectral fits, we first fitted the spectrum of region 1 with one thermal model. Using the result of this spectral fit, we obtain the normalization of the density profile for shell 1 ( $n_{\text{gas},1,1}$ ). Then, we determined the projected spectrum of shell 1 onto region 2. We fit the spectrum of region 2 with two thermal models; one is the projection of shell 1, which has been derived using equation (2) and is fixed, and the other is the spectrum of shell 2. From the result of the spectral fit, we can obtain the temperature and the density profile in shell 2 ( $i = 2$  in equation [2]). For A2107, we repeat this procedure for shell 3.

Figures 7 and 8 show the temperature and density profiles for A2670 and A2107 including projection effects. The cluster centers (cD galaxies) are cold. The discontinuities in the density profiles correspond to the boundaries of the regions for which the spectral analysis is done, and are artifacts. The error of density in the inner most region of A2670 ( $< 3''$ ) is relatively large (figure 8a) because of the uncertainties of the  $\beta$  model fit. If we assume that the density in the region is constant as is assumed in the usual deprojection analysis, the error should be smaller.

#### 4.2.2. The Comet Galaxy

The spectrum of the comet galaxy in A2670 is also affected by the projected spectrum of the outer regions of the cluster. First, we fit the surface brightness of the  $90^\circ$  sector including the comet galaxy (S1 in figure 5) with a single  $\beta$  model ( $S_{0,2} = 0$  in equation [1]) for  $106'' < R < 260''$

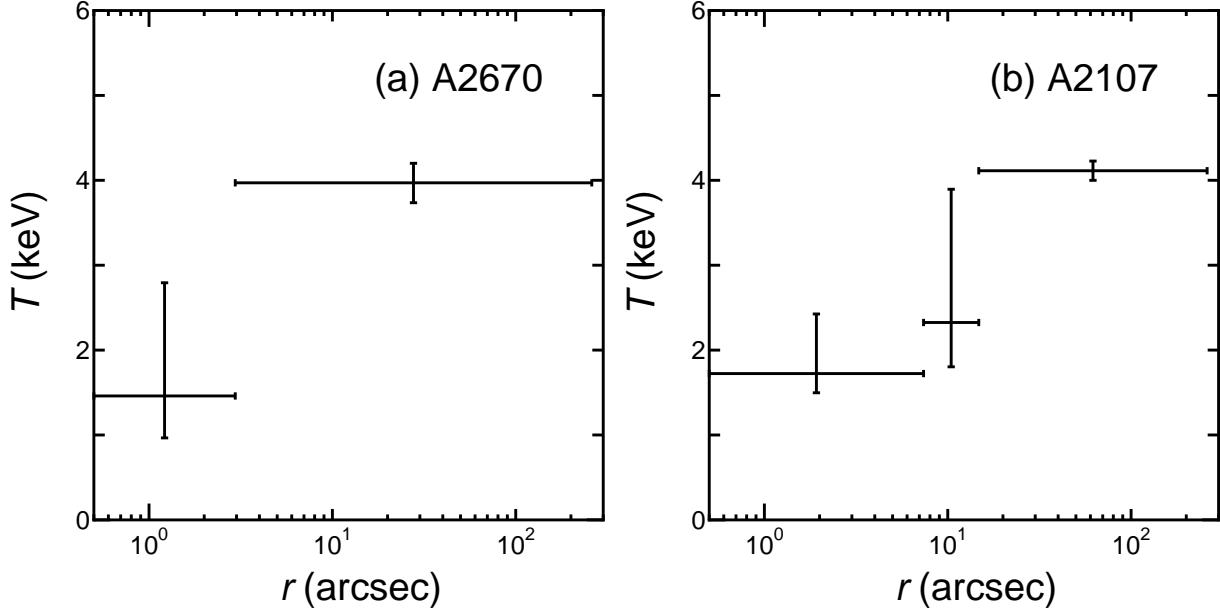


**Fig. 7.** Temperature as a function of radius for (a) A2670 excluding the  $90^\circ$  sector including the comet galaxy (S1 in figure 5) and (b) A2107.

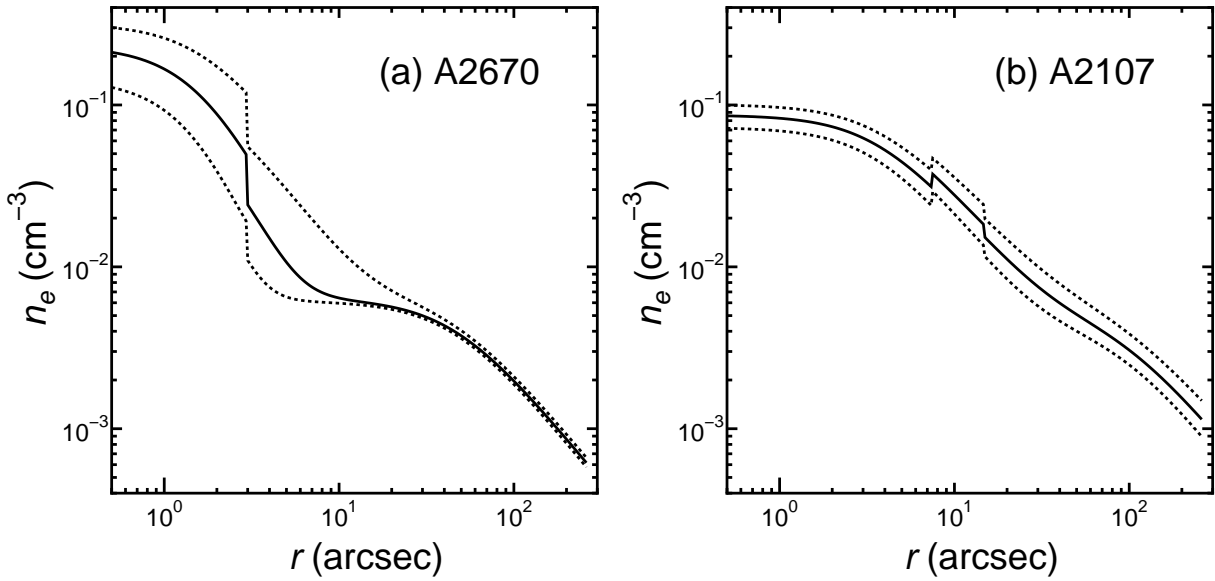


**Fig. 8.** Electron density as a function of radius for (a) A2670 excluding the  $90^\circ$  sector including the comet galaxy (S1 in figure 5) and (b) A2107. Errors are shown by dotted lines, and they are obtained by changing the parameters for  $\beta$  model fits from their best-fit values (table 1); the errors in the normalization of a thermal model (APEC) in spectral fits are also considered. The discontinuities in the figures are artifacts due to the finite regions used to determine the temperature.

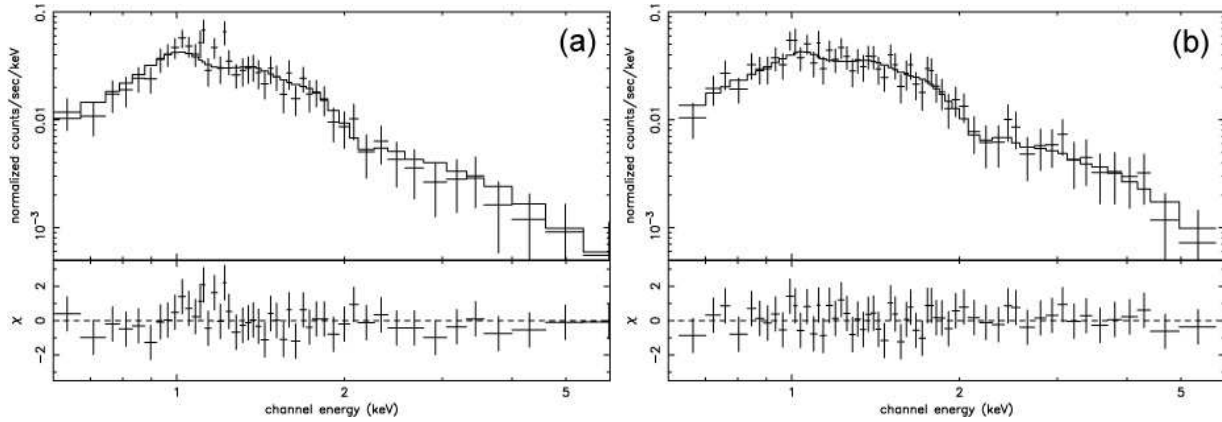


**Fig. 9.** (a) Upper panel shows the X-ray spectral data and best-fit model for the tail region (the solid rectangle in figure 5), while the lower panel plots the residuals divided by the  $1\sigma$  errors. (b) Same as (a), but the spectrum is for the surrounding  $74'' \times 49''$  rectangle (the dotted rectangle in figure 5) excluding the tail region.

from the cluster center; the inner radius is just outside the comet galaxy. Since we excluded the central region, the core radius for the single  $\beta$  fit cannot be determined. Thus, we fixed  $r_{c1}$  at the best-fit value from a single  $\beta$  model fit to the region excluding S1 while fitting  $\beta_1$  and  $S_{0,1}$  (table 1). We fit the spectrum of the fan-shaped region with one thermal model, and derive the temperature  $T_{\text{out}}$ , and the density  $n_{\text{gas},1,1}$  (equation [2]). Using the results and assuming that the cluster is spherically symmetric for  $R > 106''$ , we can estimate the projected spectrum of the outer region of the cluster on the comet galaxy region.

We fit the spectrum within the  $8''9$  circle centered on the comet galaxy (head of the comet in figure 5) with two thermal models; one of them is the spectrum of the outer region of the cluster projected on the comet galaxy and is fixed. The deprojected temperature is quite low,  $T = 1.4$  keV, if we assume that the metal abundance is the same as the ambient gas ( $Z = 0.47 Z_{\odot}$ ; table 2). This temperature is more consistent with the gas in a large galaxy or small group, rather than a cluster.

For the tail of the comet galaxy, we fit the spectrum of a  $49'' \times 22''$  rectangular region shown in figure 5 (the solid rectangle) with two thermal models. In order to consider the projection of the spectra of hotter gas surrounding the tail, we fixed the first of the two temperatures at the temperature of a surrounding  $74'' \times 49''$  rectangle (the dotted rectangle in figure 5) excluding the tail ( $T_{\text{out}}$ ). We also fixed the normalization of the hotter component at the value expected from the normalization of the spectrum of the  $74'' \times 49''$  rectangle. If we assume that the metal abundance of the tail is same as that of the ambient gas ( $Z = 0.47 Z_{\odot}$ ), the deprojected temperature of the tail is  $\sim 1.5$  keV (table 2), which is very similar to that of the galaxy at the head. If the gas were simply pulled from the galaxy, one might have expected that adiabatic expansion would have reduced the temperature further. The spectra of both regions are shown in figure 9.

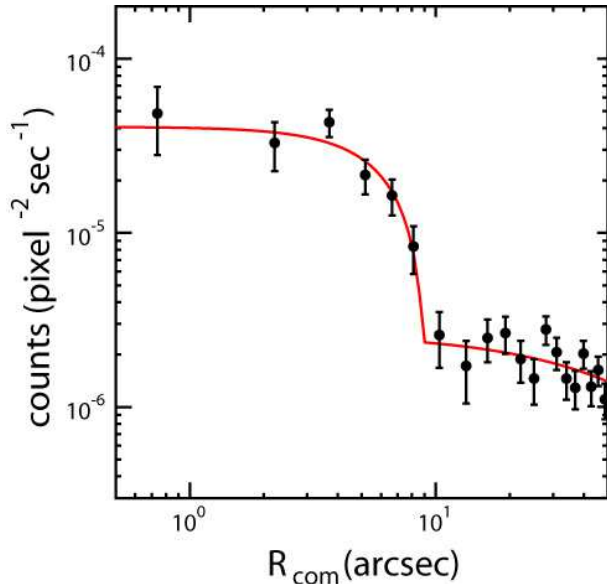


**Fig. 10.** Surface brightness as a function of the distance from the center of the comet galaxy for 0.3–10 keV for the 90° sector shown as S2 in figure 5;  $R_{\text{com}} = 0$  corresponds to the apex of the S2 region. Error bars are  $1\sigma$  Poisson uncertainties. The model fit is shown as a solid line (see text).

Since the gas in the head and tail of the comet galaxy may come from the stars in the galaxy, its metal abundance may be higher than the average value of the cluster. In table 2, we also show the results of spectral fits obtained on the assumption that the metal abundance of the gas in the head and tail is  $Z = 1 Z_{\odot}$  and that of the surrounding gas is  $Z = 0.47 Z_{\odot}$  (the cluster average). Within the errors, the results are not different from those derived on the assumption that  $Z = 0.47 Z_{\odot}$  for the head and tail.

## 5. Discussion

### 5.1. Kinematics of the Comet Galaxy

Figure 10 shows the surface brightness profile for the region in front of the comet galaxy (S2 in figure 5). The distance,  $R_{\text{com}}$ , is measured from the center of the X-ray surface brightness contour at a radius of  $\sim 8''$  from the galaxy center. The selected center is  $\sim 2''$  away from the X-ray peak because of the asymmetry of X-ray emission. At  $R_{\text{com}} = 9''$ , there is a sharp discontinuity in the X-ray surface brightness. The hardness ratio map (figure 4) suggests that there is a corresponding temperature jump (see  $T_{\text{out}}$  and  $T_{\text{in}}$  shown below), with the denser gas being cooler. The spectral fit to the comet galaxy head emission is consistent with the dense gas being quite cool. Since the brighter (higher density) region has a cooler temperature, the discontinuity appears to be a cold front, which are often observed in clusters (Markevitch et al. 2000; Vikhlinin et al. 2001b). In this subsection, we estimate the velocity of the comet galaxy from the stagnation condition at the cold front.

### 5.1.1. A Simple Case

For the sake of simplicity, we assume that the actual distance from the cluster center to the comet galaxy ( $r_{\text{gal}}$ ) is the same as the projected distance ( $b_{\text{gal}} = 143$  kpc), which is the lower boundary of the possible range ( $r_{\text{gal}} \geq b_{\text{gal}} = 143$  kpc). The ICM density profile can be derived from the result of the single  $\beta$  model fit for the fan-shaped  $106'' < R < 260''$  region in section 4.2.2 (the second line of table 1),

$$n_{\text{gas}}(r) = n_{\text{gas},1,1} [1 + (r/r_{c1})^2]^{-3\beta_1/2}, \quad (4)$$

where  $n_{\text{gas},1,1} = 9.8_{-1.1}^{+1.1} \times 10^{-2} \text{ cm}^{-3}$ . The result of the fit is shown in figure 10 (the solid line for  $R_{\text{com}} > 9''$ ). The density ahead of the galaxy is  $n_{\text{out}} = 2.0_{-0.2}^{+0.2} \times 10^{-3} \text{ cm}^{-3}$ . For the temperature outside the galaxy, we use the temperature of the fan-shaped region, which is  $T_{\text{out}} = 4.7_{-0.8}^{+1.1} \text{ keV}$ . The stagnation condition relates the pressure  $P_{\text{out}}$  far in front of the cold front with the pressure  $P_s$  at the stagnation point at the leading edge of the cold front. Because of gradients in the overall cluster density, it is difficult to determine  $P_{\text{out}}$  exactly, but it is likely to be smaller than the value determined from the product of  $n_{\text{out}}$  and  $T_{\text{out}}$  immediately in front of the comet galaxy.

Subtracting the emission around the galaxy, we found that the density inside the galaxy is almost constant at  $n_{\text{in}} = 2.8_{-0.2}^{+0.2} \times 10^{-2} \text{ cm}^{-3}$  (the solid line for  $R_{\text{com}} < 9''$  in figure 10). The temperature inside the comet galaxy is  $T_{\text{in}} = 1.4_{-0.1}^{+0.3} \text{ keV}$  (table 2). Thus, the ratio of the stagnation pressure  $P_s$  to the pressure far in front is at least  $P_s/P_{\text{out}} = 4.1_{-0.9}^{+1.3}$ . The stagnation condition depends on the Mach number of the cold front relative to the upstream gas ( $\mathcal{M}$ ) as:

$$\frac{P_s}{P_{\text{out}}} = \begin{cases} \mathcal{M}^2 \left(\frac{\gamma+1}{2}\right)^{(\gamma+1)/(\gamma-1)} \left(\gamma - \frac{\gamma-1}{2\mathcal{M}^2}\right)^{-1/(\gamma-1)} & \mathcal{M} > 1 \\ \left(1 + \frac{\gamma-1}{2}\mathcal{M}^2\right)^{\gamma/(\gamma-1)} & \mathcal{M} \leq 1 \end{cases} \quad (5)$$

where  $\gamma$  ( $=5/3$ ) is the adiabatic index (Landau, Lifshitz 1959; Vikhlinin et al. 2001b). The resulting Mach number and galaxy velocity are  $\mathcal{M} = 1.6_{-0.2}^{+0.3}$  and  $v_{\text{gal}} = 1.7_{-0.3}^{+0.4} \times 10^3 \text{ km s}^{-1}$ . Since the values of  $r_{\text{gal}}$  and  $P_s/P_{\text{out}}$  we adopted are the lower limits, the values of  $\mathcal{M}$  and  $v_{\text{gal}}$  are also the lower limits.

### 5.1.2. Ram-Pressure Stripping

Ram-pressure stripping can have a strong influence on the evolution of galaxies in clusters (Gunn, Gott 1972; Fujita, Nagashima 1999; Fujita 2001). The morphology of the comet galaxy suggests that the galaxy is affected by ram-pressure stripping. A similar galaxy is found in A2125 (Wang et al. 2004). If the comet galaxy is at  $r_{\text{gal}} = b_{\text{gal}}$  (see section 5.1.1), the ram-pressure on the comet galaxy from the outside ICM ( $P_{\text{ram}} = \rho_{\text{out}} v_{\text{gal}}^2$ , where  $\rho_{\text{out}}$  is the mass density corresponding to  $n_{\text{out}}$ ) is  $P_{\text{ram}} = 1.2_{-0.3}^{+0.5} \times 10^{-10} \text{ g cm}^{-1} \text{ s}^{-2}$ , based on the velocity derived above and the cluster gas density profile.

The gas in the comet galaxy would be stripped when the ram-pressure becomes larger than the static pressure of the galaxy:

$$P_{\text{ram}} > P_{\text{gal}} \equiv \rho_{\text{in}} \frac{k_{\text{B}} T_{\text{in}}}{\mu m_{\text{p}}}, \quad (6)$$

where  $\rho_{\text{in}}$  is the mass density corresponding to  $n_{\text{in}}$ ,  $k_{\text{B}}$  is the Boltzmann constant,  $\mu$  ( $=0.6$ ) is the mean molecular weight, and  $m_{\text{p}}$  is the proton mass (Nulsen 1982; Mori, Burkert 2000; Sarazin 2002). Since  $P_{\text{gal}} = 1.2_{-0.1}^{+0.2} \times 10^{-10} \text{ g cm}^{-1} \text{ s}^{-2}$ , the comet galaxy marginally satisfies the condition (6).

### 5.2. The Origin of the Gas around the Comet Galaxy

In this subsection, we consider whether the gas around the comet galaxy can be supplied from the stars in the galaxy. The  $B$ -band absolute magnitude of the comet galaxy is  $-21.3^2$ . Since the stellar mass-loss rate per unit  $B$ -band luminosity is given by  $\dot{m}_{\star} \approx 1.5 \times 10^{-11} M_{\odot} \text{ yr}^{-1} L_{\odot}^{-1}$  (Faber, Gallagher 1976), the total mass-loss rate of the comet galaxy is  $\dot{M}_{\star} \approx 0.81 M_{\odot} \text{ yr}^{-1}$ . Since the mass of the gas in the comet galaxy (the head of the comet) is  $M_{\text{gal,gas}} = 7.2_{-0.4}^{+0.4} \times 10^9 M_{\odot}$ , the gas would be supplied by the stars over the time  $t_{\star} = M_{\text{gal,gas}}/\dot{M}_{\star} \approx 8.9 \times 10^9 \text{ yr}$ . The time-scale is marginally smaller than the age of the Universe, and thus the gas could be supplied by the stars. However, we did not include the gas stripped from the comet galaxy in this estimate. Assuming that the tail of the comet galaxy is roughly a cylinder with a radius of 16 kpc and the length of 71 kpc (the tail region shown in figure 5), the gas mass of the tail is  $1.5 \times 10^{10} M_{\odot}$ , which is larger than  $M_{\text{gal,gas}}$ . Since the temperature of the tail is much smaller than that of the surrounding region ( $\sim 4 \text{ keV}$ ; table 2), most of the gas came from the comet galaxy. This means that most of the gas around the comet galaxy (head and tail;  $\sim 2.2 \times 10^{10} M_{\odot}$ ) did not originate in the stars in this galaxy at present day loss rates, although there is uncertainty of the mass loss rate especially at the early phase of galaxy evolution. The comet galaxy probably was the central galaxy of a small cluster or group, and the gas around it probably originated as intracluster or intragroup medium.

We note that the above conclusion does not depend on the assumed metal abundance of the gas in the head and tail of the galaxy ( $Z = 0.47 Z_{\odot}$ ). Even if we assume that the metal abundance of the gas in the head and tail is higher than the surrounding gas and is  $Z = 1Z_{\odot}$ , their gas masses are reduced by only  $\sim 15\%$ .

We also consider the case where the tail is clumpy. Here, we assume that the tail is isothermal but consists of two different density gas,  $\rho_1$  and  $\rho_2$ . The gas with density  $\rho_1$  fills the volume  $fV_{\text{tail}}$  and that with density  $\rho_2$  fills the volume  $(1-f)V_{\text{tail}}$ , where  $V_{\text{tail}}$  is the total volume of the tail and  $f$  is the parameter ( $0 \leq f \leq 1$ ). If  $\rho_1 \gg \rho_2$ , the luminosity of the tail is given by  $L_{\text{tail}} \propto \rho_1^2 f V_{\text{tail}}$ . On the other hand, if we assume that the tail is uniform (the density is  $\rho_0$  and the mass is  $M_{\text{tail},0} = \rho_0 V_{\text{tail}}$ ), the luminosity is represented by  $L_{\text{tail}} \propto \rho_0^2 V_{\text{tail}}$ . Thus, for a given  $L_{\text{tail}}$ , the density of the clumps is written as  $\rho_1 = \rho_0 f^{-1/2}$ , and the mass of the clumpy tail is approximately given by  $M_1 = \rho_1 f V_{\text{tail}} = M_0 f^{1/2}$ . This means that if the tail is highly clumpy,

<sup>2</sup> NED: <http://nedwww.ipac.caltech.edu/>



the tail mass could be smaller than that derived above ( $M_{\text{tail},0} = 1.5 \times 10^{10} M_{\odot}$ ). However, such clumps would easily be destroyed through hydrodynamical interactions with the surrounding gas (e.g. Mathews 1990).

### 5.3. The cD Galaxies of A2670 and A2107

From the hardness ratio maps (figure 4) and surface brightness profiles (figure 6), we know that the cool, dense interstellar medium (ISM) of A2670 and A2107 is confined within  $3''$  and  $15''$  from the galaxy centers (X-ray peaks), respectively. The pressure ratio at the boundary is  $P_{\text{ISM}}/P_{\text{ICM}} = 0.7_{-0.4}^{+0.9}$  for A2670 and  $0.7_{-0.2}^{+0.5}$  for A2107. Thus the pressure is consistent with being continuous at the boundary. The allowable velocities derived from a stagnation condition (equation [5]) are  $\lesssim 1400 \text{ km s}^{-1}$  for A2670 and  $\lesssim 1000 \text{ km s}^{-1}$  for A2107. Since these limits are still much larger than the observed radial peculiar velocities of the cDs in their clusters ( $v_{\text{P}} = 433 \text{ km s}^{-1}$  for A2670, and  $270 \text{ km s}^{-1}$  for A2107; Oegerle, Hill 2001), these limits are not very constraining.

The ISM masses are  $M_{\text{ISM}} = 7.8_{-2.9}^{+2.9} \times 10^8 M_{\odot}$  and  $5.5_{-0.9}^{+0.9} \times 10^9 M_{\odot}$  for A2670 and A2107, respectively. In this estimation, we assumed that the metal abundance of the ISM is the same as the cluster average. If we assume that the metal abundance of the ISM is  $Z = 1 Z_{\odot}$  as in the case of the comet galaxy, the ISM masses are reduced by only  $\lesssim 15\%$ , which does not affect the following discussion. The  $B$ -band absolute luminosities of the cD galaxies are  $-22.7$  and  $-21.6$  for A2670 and A2107, respectively. As we did for the comet galaxy, we derive the time-scale for the stars in the cD galaxies to supply the ISM. For A2670,  $t_{\star} = 2.8 \times 10^8 \text{ yr}$ , and for A2107,  $t_{\star} = 5.1 \times 10^9 \text{ yr}$ . The time-scales are smaller than or comparable to the typical age of a cluster ( $\sim 3\text{--}10 \text{ Gyr}$ ; e.g. Kitayama, Suto 1996). On the other hand, only a small fraction of the stellar mass loss would occur within the small volume occupied by the cooler gas today. Thus, stellar mass loss would only be adequate if the gas was ejected before the cD galaxies were located in their present environment, and the ISM was compressed by the high ICM pressure to its current small volume. In any case, the cooling times of the ISM are  $t_{\text{cool}} = 2.7_{-1.4}^{+2.8} \times 10^8 \text{ yr}$  for A2670, and  $8.3_{-2.2}^{+5.9} \times 10^8 \text{ yr}$  for A2107. Thus, while stars in the cD can marginally supply the ISM before cooling becomes effective for A2670, they cannot for A2107.

For A2670, the size of the ISM region is comparable to those of NGC 4874 and 4889 in the Coma cluster ( $\sim 3 \text{ kpc}$ ; Vikhlinin et al. 2001a). Both A2670 and Coma are merging clusters. Thus, a compact ISM may be common for merging clusters. For the two galaxies in Coma, it has been shown that  $t_{\text{cool}} < t_{\star}$  and some heating source is required to prevent radiative cooling (Vikhlinin et al. 2001a). Since  $t_{\text{cool}} \approx t_{\star}$ , the ISM of the cD galaxy in A2670 may also be affected by the heating source. Although the size of the ISM region is larger ( $12 \text{ kpc}$ ), radiative cooling must be suppressed as well for A2107 ( $t_{\text{cool}} < t_{\star}$ ). These observations show the similarity between ‘cooling flow’ clusters and dynamically young merging clusters in terms of the necessity of some heating sources. For the dynamically young clusters, active galactic

nuclei (AGNs) are not good candidates for heating sources because AGN jets would deposit their energy outside the small ISM regions (e.g. Omma et al. 2004). Thus, as discussed by Vikhlinin et al. (2001a), thermal conduction may be the heating source. In fact, the time-scales of the thermal conduction are short;  $t_{\text{cond}} \approx 8.5 \times 10^6$  yr for A2670, and  $1.9 \times 10^7$  yr for A2170, which are derived using equation (9) in Fujita and Goto (2004). Note that the saturation of thermal conduction is generally not important for cD galaxies because the electron density is high around them. Since  $t_{\text{cond}} \ll t_*$ , thermal conduction can supply enough energy to the ISM. On the other hand, at least for A2107, the ISM structure seen in the surface brightness map (figure 2b) and that seen in the hardness ratio map (figure 4b) are different. This indicates that the ISM is not in pressure equilibrium, which may be due to the dynamical motion around the galaxy. Cluster mergers may induce such motion, which may finally lead to turbulence and heat the cluster core through the turbulent mixing as is shown in the ‘tsunami’ model (Fujita et al. 2004; Fujita et al. 2005).

## 6. Conclusions

We present an analysis of Chandra observations of the galaxy clusters A2670 and A2107. The peculiar velocities of the cD galaxies are unusually large ( $> 200 \text{ km s}^{-1}$ ) and the clusters are undergoing mergers. To the west of the cD galaxy of A2670, we find a galaxy having a comet-like X-ray structure (comet galaxy). The leading edge of the structure is a cold front. From the pressure profile across the cold front, we estimate the velocity of the galaxy in the cluster A2670. The mass of X-ray gas in the comet-like structure is too large to have been produced by stellar mass loss within the galaxy itself. Thus, it is likely that the galaxy was at the center of a small cluster or group, and that its intracluster or intragroup medium is being stripped by ram-pressure. The sizes of the cooler, X-ray interstellar medium (ISM) regions of the cD galaxies in A2670 and A2107 are very small. This is similar to the brightest galaxies in the Coma cluster, which is also a merging cluster. Since the cooling time of the ISM is small, there must be some heating sources in the galaxies. The compactness of the ISM indicates that the heating sources are not the AGNs in the galaxies. We suggest thermal conduction or hydrodynamical heating by ‘tsunamis’ as possible heat sources to balance the observed X-ray emission.

We are grateful to Tracy Clarke for useful comments. Y. F. is supported in part by a Grant-in-Aid from the Ministry of Education, Culture, Sports, Science, and Technology of Japan (14740175). Support for this work was provided by the National Aeronautics and Space Administration primarily through Chandra award GO4-5137X, but also through GO4-5133X, GO4-5149X and GO4-5150X, issued by the Chandra X-ray Observatory, which is operated by the Smithsonian Astrophysical Observatory for and on behalf of NASA under contract NAS8-39073. G. R. S. acknowledges the receipt of an ARCS fellowship.

## References

- Bird, C. 1994, *ApJ*, 422, 480
- Blanton, E. L., Sarazin, C. L., McNamara, B. R., & Wise, M. W. 2001, *ApJL*, 558, L15
- Buote, D. A. & Tsai, J. C. 1996, *ApJ*, 458, 27
- David, L. P., Slyz, A., Jones, C., Forman, W., Vrtillek, S. D., & Arnaud, K. A. 1993, *ApJ*, 412, 479
- Faber, S. M., & Gallagher, J. S. 1976, *ApJ*, 204, 365
- Fujita, Y. 2001, *ApJ*, 550, 612
- Fujita, Y., & Goto, T. 2004, *PASJ*, 56, 621
- Fujita, Y., Matsumoto, T., & Wada, K. 2004, *ApJL*, 612, L9
- Fujita, Y., Matsumoto, T., Wada, K., & Furusho, T. 2005, *ApJL*, 619, L139
- Fujita, Y., & Nagashima, M. 1999, *ApJ*, 516, 619
- Fujita, Y., Sarazin, C. L., Kempner, J. C., Rudnick, L., Slee, O. B., Roy, A. L., Andernach, H., & Ehle, M. 2002, *ApJ*, 575, 764
- Fukazawa, Y., Makishima, K., Tamura, T., Nakazawa, K., Ezawa, H., Ikebe, Y., Kikuchi, K., & Ohashi, T. 2000, *MNRAS*, 313, 21
- Furusho, T., Yamasaki, N. Y., & Ohashi, T. 2003, *ApJ*, 596, 181
- Gunn, J. E., & Gott, J. R. I. 1972, *ApJ*, 176, 1
- Hobbs, I. S., & Willmore, A. P. 1997, *MNRAS*, 289, 685
- Johnstone, R. M., Allen, S. W., Fabian, A. C., & Sanders, J. S. 2002, *MNRAS*, 336, 299
- Kaastra, J. S., Ferrigno, C., Tamura, T., Paerels, F. B. S., Peterson, J. R., & Mittaz, J. P. D. 2001, *A&A*, 365, L99
- Kawano, N., Ohto, A., & Fukazawa, Y. 2003, *PASJ*, 55, 585
- Kitayama, T., & Suto, Y. 1996, *ApJ*, 469, 480
- Landau, L. D., & Lifshitz, E. M. 1959, *Fluid Mechanics*, § 114 (London: Pergamon)
- Makishima, K. et al. 2001, *PASJ*, 53, 401
- Markevitch, M. et al. 2000, *ApJ*, 541, 542
- Mathews, W. G. 1990, *ApJ*, 354, 468
- Mazzotta, P., Edge, A. C., & Markevitch M. 2003, *ApJ*, 596, 190
- Mori, M. & Burkert, A. 2000, *ApJ*, 538, 559
- Nulsen, P. E. J. 1982, *MNRAS*, 198, 1007
- Oegerle, W. R., & Hill, J. M. 2001, *AJ*, 122, 2858
- Omma, H., Binney, J., Bryan, G., & Slyz, A. 2004, *MNRAS*, 348, 1105
- Peterson, J. R. et al. 2001, *A&A*, 365, L104
- Stark, A. A., Gammie, C. F., Wilson, R. W., Bally, J., Linke, R. A., Heiles, C., & Hurwitz, M. 1992, *ApJS*, 79, 77
- Sarazin, C. L. 2002, in *Merging Processes in Galaxy Clusters*, ed. L. Feretti, L. M. Gioia, & G. Giovannini (Astrophysics and Space Science Library, 272), 1
- Tamura, T. et al. 2001, *A&A*, 365, L87
- Vikhlinin, A., Markevitch, M., Forman, W., & Jones, C. 2001a, *ApJL*, 555, L87
- Vikhlinin, A., Markevitch, M., & Murray, S. S. 2001b, *ApJ*, 551, 160

- Vikhlinin, A., Markevitch, M., Murray, S. S., Jones, C., Forman, W., & Van Speybroeck, L. 2005, ApJ, 628, 655
- Wang, Q. D., Owen, F., & Ledlow, M. 2004, ApJ, 611, 821
- White, D. A., Jones, C., & Forman, W. 1997, MNRAS, 292, 419